Strain-tuned spin polarization and optical conductivity in MoS_2/EuS heterostructures

Dan-Na Liu and Yong Guo*

Department of Physics and State Key Laboratory of Low-Dimensional Quantum Physics, Tsinghua University, Beijing 100084, People's Republic of China

(Received 6 October 2022; revised 9 February 2023; accepted 13 February 2023; published 21 February 2023)

We investigate strain-tuned spin transport and optical conductivity in a monolayer (ML) *n*-type MoS_2/EuS heterostructure under linearly polarized terahertz radiation using a low-energy effective Hamiltonian, which takes displacement of the Dirac point induced by strain into account. Through modifying the strain modulus, we find an adjustable relationship between the band edge energy and the strain. Thus the threshold and range of allowed angles are strongly dependent on the strength of strain ϵ, whereas the angle θ along which the strain is applied only acts on the former. Due to spin-flipped scattering generated by Rashba spin-orbit coupling, the in-plane spin polarizations (i.e., P_X and P_Y) can be achieved, and their intensity can be enhanced by increasing ϵ. Interestingly, we find that the out-of-plane spin polarization (i.e., P_Z) is related to the synergy of ϵ and the Rashba parameter λ_R. Especially, P_Z can approach 100% when $\epsilon = 9\%$ and $\lambda_R = 2$ meV. Furthermore, the optical transition between the spin-splitting subbands of the conduction band under the strain is studied. It is shown that by varying ϵ we can control the magnitude of both absorption peaks and absorption valleys in optical conductivity. Moreover, the presence of λ_R can be used to further enhance the absorption peaks and valleys because λ_R can tune the energy difference between the spin-splitting subbands within a specific valley and thus affect the optical transition channels. Our findings demonstrate that the strain can influence the tunneling behavior and valley Hall conductivity in a ML *n*-type MoS_2/EuS heterostructure, and these features are applicable to other two-dimensional ML transition metal dichalcogenides, which is promising for terahertz and valleytronic devices.

DOI: 10.1103/PhysRevB.107.075430

I. INTRODUCTION

Exploiting the valley pseudospin of electrons to encode and process information, that is, valleytronics, is a parallel concept to spintronics. Unlike conventional semiconductors with multiple valleys, for example, silicon, valleys in two-dimensional (2D) materials are practically binary quantum degrees of freedom that can be selectively detected. Monolayer (ML) transition metal dichalcogenides (TMDs) have attracted extensive exploration because of their contribution to significantly advancing the investigation of valleytronics [1–3]. Owing to the lack of an in-plane inversion center, the ML TMD features two degenerate but inequivalent valleys at the corners of the first Brillouin zone [4,5], i.e., the K and K' points. Breaking inversion symmetry makes carriers with opposite valley indexes possess opposite Berry curvature Ω and orbit magnetic moment $\mathbf{m}$. The coupling of Ω and the in-plane electric field gives rise to the anomalous velocity which is associated with the valley Hall effect (VHE) [6–9]. Besides, $\mathbf{m}$ renders energy displacement which is related to the physical phenomenon of the optical selection rule in the presence of a magnetic field [10–13].

Because the essence of the connection between valleys in 2D materials with hexagonal lattice structure is through time-reversal symmetry, Hall currents from different valleys under the driving force of an electromagnetic field have equal magnitudes but opposite directions [13]. Thus the net Hall current vanishes completely [14]. The major challenge is to find feasible approaches to lift the valley degeneracy. Circularly polarized light [15–18], a magnetic field [19], and magnetic doping [20] have been demonstrated to break the balance of carrier densities between the two inequivalent valleys. However, optical pumping is not applicable for valley filtering because it is difficult to control accurately [21]. On the other hand, a tiny valley splitting of 0.1–0.2 meV/T makes magnetic control feasible only under a strong field, which is difficult to apply in practice [19,22,23]. Furthermore, the ability to use magnetic doping to control valley pseudospin is limited due to the scattering of electrons by impurities [24].

Beyond the abovementioned strategies, constructing a vertical heterostructure formed by a TMD and a ferromagnetic insulator such as EuS [25,26], CrI_3 [27], MnO [24,28,29], $YMnO_3$ [30], and EuO [31] is a more advantageous means, which can achieve giant valley splitting by exploiting the magnetic proximity effect. Theoretically, generation of giant and tunable valley splitting of 44 meV has been predicted in a monolayer $MoTe_2$ system based on EuO substrates [32]. Experimentally, Zhao *et al.* demonstrated the greatly enhanced valley splitting in a monolayer WSe_2/EuS heterostructure and achieved a valley splitting of 25 meV, which is equivalent to an effective exchange field of 12 T [26]. In addition, the strength of valley splitting can be further promoted by the in-plane strain [21,33]. Together with the preponderance of a high Young's modulus [34] and elastic limit [35], ML MoS_2 is a flexible and soft material, which can withstand significant

*guoy66@tsinghua.edu.cn

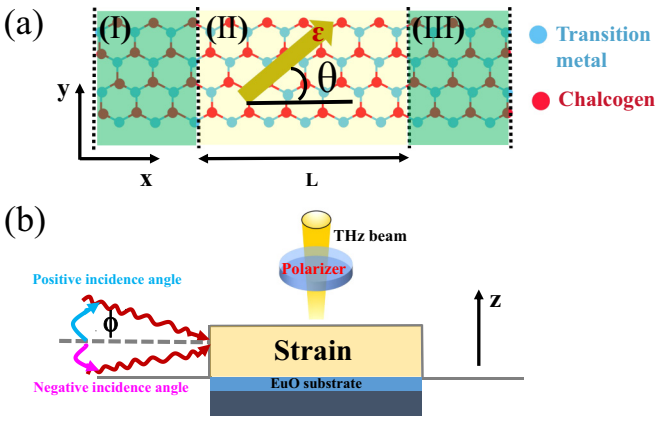

FIG. 1. (a) Schematic of the proposed model. Regions I and III represent the pure monolayer (ML) MoS_2 regions. Region II corresponds to the strained MoS_2/EuS region, in which a vertical electric field and a relatively weak terahertz (THz) radiation field linearly polarized along the 2D MoS_2 plane are applied. The selected x axis is parallel to the zigzag direction of the MoS_2 sheet, and the direction of the uniform planar tension is θ. (b) Energy potential profile of the strained MoS_2/EuS heterostructure with gate voltage modulation, which is sandwiched between two pure MoS_2 MLs. ϕ is the incident angle, and the region of positive (negative) incidence angles is defined as the area in the clockwise (counterclockwise) direction relative to the normal incidence.

strain without rupture [34,36–38]. The valley splitting induced by strain in TMDs has been investigated both experimentally [39] and theoretically [40]. Moreover, recent studies have shown that linearly polarized terahertz irradiation can be used as an advanced technology to observe the VHE, when a ML 2D material is placed on ferromagnetic substrates [14,41].

In this paper, we theoretically apply uniaxial strain for investigation of the VHE in a ML n-type MoS_2/EuS heterostructure under linearly polarized terahertz irradiation. Our major motivation is to explore how the strain regulates the transport properties without and with spin flip and the optical Hall conductivity with spin-flip interband transition within the conduction band.

In Sec. II, we specify the Hamiltonian in the presence of both proximity interaction and strain terms, and in Sec. III we present the numerical results and relevant analysis of the band structures and transport properties. In Sec. IV, we discuss the strain-tuned spin polarization components, and the optical conductivity under strain is investigated in Sec. V. Conclusions follow in Sec. VI.

II. THEORETICAL MODEL

We construct a MoS_2/EuS heterostructure with a strained ML MoS_2 placed on a EuS substrate, as shown in Fig. 1. The Hamiltonian for unstrained ML MoS_2 considering the proximity-induced interaction is [32]

$$H = \left[at(\tau k_x\hat{\sigma_x} + k_y\hat{\sigma_y}) + \frac{\Delta}{2}\hat{\sigma_z} + U\right]\otimes\hat{I} + \tau(\lambda_c\hat{\sigma_+} + \lambda_v\hat{\sigma_-})\otimes\hat{s_z} + \lambda_R(\tau\hat{\sigma_x}\otimes\hat{s_y} - \hat{\sigma_y}\otimes\hat{s_x}) - (B_c\hat{\sigma_+} + B_v\hat{\sigma_-})\otimes\hat{s_z}. \quad (1)$$

Here, the first part corresponds to the orbit interaction, where $a = 3.193$ Å and $t = 1.1$ eV are the representatives of the lattice constant and hopping parameter, respectively [42]. $\tau = \pm 1$ are the valley indexes, $k_{x(y)}$ are the wave vectors, $\Delta = 1.66$ eV is the band gap, and U is the electrostatic potential energy induced by a vertical electric field. The second contribution is to describe the effective spin-orbit coupling with $\lambda_c = 1.5$ ($\lambda_v = 75$) meV. Also, $\hat{\sigma_i}$ and $\hat{s_i}$ ($i = x, y, z$) are the Pauli matrices referring to orbit pseudospin and real spin, respectively. $\hat{I}$ is the unit matrix, and $\hat{\sigma_\pm} = (\hat{\sigma_0} \pm \hat{\sigma_z})/2$. The third term originates from the substrate and perpendicular electric field, and λ_R is the Rashba coupling parameter [43]. It is worth noting that λ_R generally contains three contributions: (1) λ_R often exists in 2D hexagonal crystals with uniaxial symmetry [44,45]. (2) It has been proved that λ_R can be adjusted by a perpendicular electric field and determined by *ab initio* calculations or by fitting with experimental data. Slobodeniuk and Basko [46] obtained the relation $\lambda_R = \alpha_R\Delta/(2at)$ with α_R being the Rashba parameter [47]. (3) λ_R can be further enhanced by the inversion-symmetry-breaking field perpendicular to the plane of the monolayer TMD when the monolayer TMD is placed on a substrate [26,32]. B_c and B_v are effective Zeeman fields acting on the conduction and valence bands of MoS_2, respectively, which are generated by the exchange coupling with the substrate.

We are interested in the situation where the ML MoS_2 sheet is uniformly stretched (or compressed) along a prescribed direction, as shown in Fig. 1(a). The Cartesian system is selected in such a way that the x axis is consistent with the zigzag direction of the lattice. The strain tensor in the lattice coordinate system is written as [48–50]

$$\boldsymbol{\epsilon} = \epsilon\begin{pmatrix}\cos^2\theta - \nu\sin^2\theta & (1+\nu)\sin\theta\cos\theta \\ (1+\nu)\sin\theta\cos\theta & \sin^2\theta - \nu\cos^2\theta\end{pmatrix}, \quad (2)$$

where ϵ denotes the strain modulus and $\nu = 0.21$ is the Poisson's ratio for MoS_2 [49]. θ represents the angle of applied strain with respect to the x axis, and we set the x axis to coincide with the zigzag direction. According to the tight-binding model, strain can influence the electronic properties by the derivative of the hopping parameter with respect to the lattice vector [50]. By extending the tight-binding Hamiltonian in the strain modulus, we find that the low-energy approximation of the Hamiltonian can still be expressed in Dirac-like form [51,52]:

$$H = \left[at(\tau q_x\tilde{\sigma_x} + q_y\tilde{\sigma_y}) + \frac{\Delta}{2}\hat{\sigma_z}\right]\otimes\hat{I} + \tau(\lambda_c\hat{\sigma_+} + \lambda_v\hat{\sigma_-})\otimes\hat{s_z} + \lambda_R(\tau\hat{\sigma_x}\otimes\hat{s_y} - \hat{\sigma_y}\otimes\hat{s_x}) - (B_c\hat{\sigma_+} + B_v\hat{\sigma_-})\otimes\hat{s_z}, \quad (3)$$

where $\boldsymbol{q} = (q_x, q_y)^T = \boldsymbol{k} - \boldsymbol{q}_D$ denotes the wave vector. $\boldsymbol{q}_D$ represents the pseudovector potential, satisfying $\boldsymbol{q}_D a = \tau(\kappa_0\varepsilon(1+\nu)\cos(2\theta), -\kappa_0\varepsilon(1+\nu)\sin(2\theta))^T$. $\tilde{\sigma_i} = \epsilon_i\sigma_i$ ($i = x, y$), with $\epsilon_i = 1 - \lambda_i\epsilon$, $\lambda_x = 2(\kappa_0 - 1/2)$, and $\lambda_y = -2(\kappa_0 - 1/2)\nu$. $\kappa_0 = (a/2t)|\partial t/\partial a| \approx 1.6$ indicates the logarithmic derivative of the nearest-neighbor parameter t to the lattice constant a in the absence of strain. The Hamiltonian

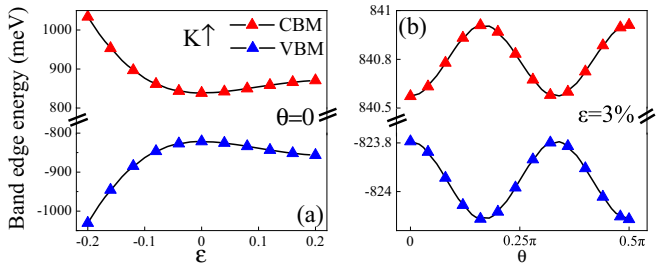

FIG. 2. The band edge energy as a function of (a) ϵ when $\theta = 0\pi$ and (b) θ when $\epsilon = 3\%$.

is equivalent to a 4×4 matrix

$$H = \begin{bmatrix} \frac{\Delta}{2} + h_\tau^c & 0 & \tau\Lambda_x - i\Lambda_y & 0 \\ 0 & \frac{\Delta}{2} - h_\tau^c & 2i\lambda_R & \tau\Lambda_x - i\Lambda_y \\ \tau\Lambda_x + i\Lambda_y & -2i\lambda_R & -\frac{\Delta}{2} + h_\tau^v & 0 \\ 0 & \tau\Lambda_x + i\Lambda_y & 0 & -\frac{\Delta}{2} - h_\tau^v \end{bmatrix}, \tag{4}$$

where

$$h_\tau^{c(v)} = \tau\lambda_{c(v)} - B_{c(v)},$$
$$\Lambda_i = at\epsilon_i q_i. \tag{5}$$

It is convenient to refer to the direction of strain as the x axis, which requires the rotation of the Dirac equation in the sublattice space by using unitary matrix [53,54]

$$U(\theta) = \begin{pmatrix} 1 & 0 \\ 0 & e^{-i\theta} \end{pmatrix}; \tag{6}$$

one obtains

$$H = U^\dagger(\theta) H U(\theta). \tag{7}$$

The position of the Dirac points after rotation is $\mathbf{q}_D a = \tau(\kappa_0\epsilon(1+\nu)\cos(3\theta), -\kappa_0\epsilon(1+\nu)\sin(3\theta))^T$. The transmission coefficient $t_{\tau,ss'}$ and eigenvalue can be derived from the strained Hamiltonian, and details of the relevant derivation are contained in Appendix A.

III. TRANSPORT PROPERTIES

First, we investigate the effect of strain on the transport properties of electron tunneling through the above system, and the derivations for wave equations and transmission probability are given in Appendix A. Figure 2 presents the effects of the strength of strain ϵ and the angle along which the strain is applied, θ, on the band edge energy. It is clearly demonstrated that the band edge energy strongly depends on strain. For the case of $\theta = 0$ [see Fig. 2(a)], the band edge energy of the conduction band minimum (CBM) initially decreases with ϵ from a value of 1033 meV and reaches its minimum value of 838.5 meV at 0% strain; then it rises with the further increase of ϵ. Conversely, with an increase in ϵ, the band edge energy of the valence band maximum (VBM) first increases to its maximum value and then decreases. Correspondingly, the band gap reaches a minimum value of 1660 meV in the relaxed situation ($\epsilon = 0\%$) and a maximum value of 2064 meV at -20% strain. Figure 2(b) gives the band edge energies as a function of θ when $\epsilon = 3\%$. It demonstrates that both the CBM and the VBM oscillate with θ and that the corresponding band gap is also sensitive to θ. Especially, at $\theta = 0\pi$ and $\theta = 0.5\pi$, the band gap reaches a minimum value of 1664 meV and a maximum value of 1665 meV, respectively.

Figure 3 shows the isoenergy surfaces (ISs) in the strained region (colored circles) and the unstrained region (black circles for the K valley and gray circles for the K' valley) under various strain and gate voltage configurations, i.e., (ϵ, U(meV)). It is clear that the transmission segment is asymmetric with respect to $\phi = 0$. As ϵ increases from -3 to 3%, the IS in the K valley of the strained region moves downward, while the IS in the K' valley moves upward. The conservation of the k_y component of the wave vector and the fact that k_x corresponding to the propagating wave is a real value determine the range of incident angles that are not being filtered out by the strained region. For example, when $\epsilon = -3\%$ and $U = 100$ meV, the overlap between the unstrained isoenergy surface and the strained one for the K valley with spin up ($K\uparrow$) yields a range of $k_y \in (-0.0283, 0.05375)$ Å^{-1}, which corresponds to the red shaded region in Fig. 3(a). As shown in Fig. 1(b), the incident angle along the clockwise direction relative to the normal incidence is defined as the positive incidence angle, while the angle along the counterclockwise direction is defined as the negative incidence angle. In such a way, the maximum of the positive incidence angle that can transmit the structure is $\phi_1 = \arctan(0.053\,75/0.116) \approx 25^\circ$ [see point A in Fig. 3(a)], while the minimum value of the negative incidence angle is $\phi_1 = \arctan(-0.0283/0.125) \approx -13^\circ$ [see point B in Fig. 3(a)]. Therefore the threshold of the allowed angles for an electron with $K\uparrow$ and without spin flip when $\epsilon = -3\%$ and $U = 100$ meV is $(-13^\circ, 25^\circ)$, which will be confirmed in the transmission spectrum and we will discuss later [see Fig. 4(a)].

The selection rule of ϵ on the allowed angle is well illustrated in Fig. 3: (1) For the K valley, the angular range for generating propagating waves narrows when $\phi \subset [0, \pi/2]$, while the range widens when $\phi \subset [-\pi/2, 0]$ with increasing ϵ [see Figs. 3(a) and 3(b)]. (2) For the K' valley, the situation is quite opposite, i.e., the angular range widens when $\phi \subset [0, \pi/2]$, whereas the range narrows when $\phi \subset [-\pi/2, 0]$ as ϵ increases [see Figs. 3(c) and 3(d)]. These results clearly show the obvious difference in band structures between the two valleys under strain and indicate that the heterostructure has the function of filtering valley particles.

The influence of electrostatic potential U on the allowed angles for obvious transport when ϵ is fixed is also shown in Fig. 3. As U is decreased to 10 meV when $\epsilon = 3\%$ (purple circles), the ISs of the strained region in the K valley shift downward relative to the unrelaxed ones [see Figs. 3(a) and 3(b)], while the ISs move upward in the K' valley [see Figs. 3(c) and 3(d)], which results are consistent with the trend of the ISs when (3%, 100). In addition, the IS of (3%, 10) has the radius closing to the unstrained one. In such a case, k_y of the strained regions for the K (K') valley almost overlaps with that of the unstrained one, which results in the transmission of particles with almost all incident angles.

Figures 3(e)–(h) show the strained and unstrained band structures near the Dirac point for different configurations of

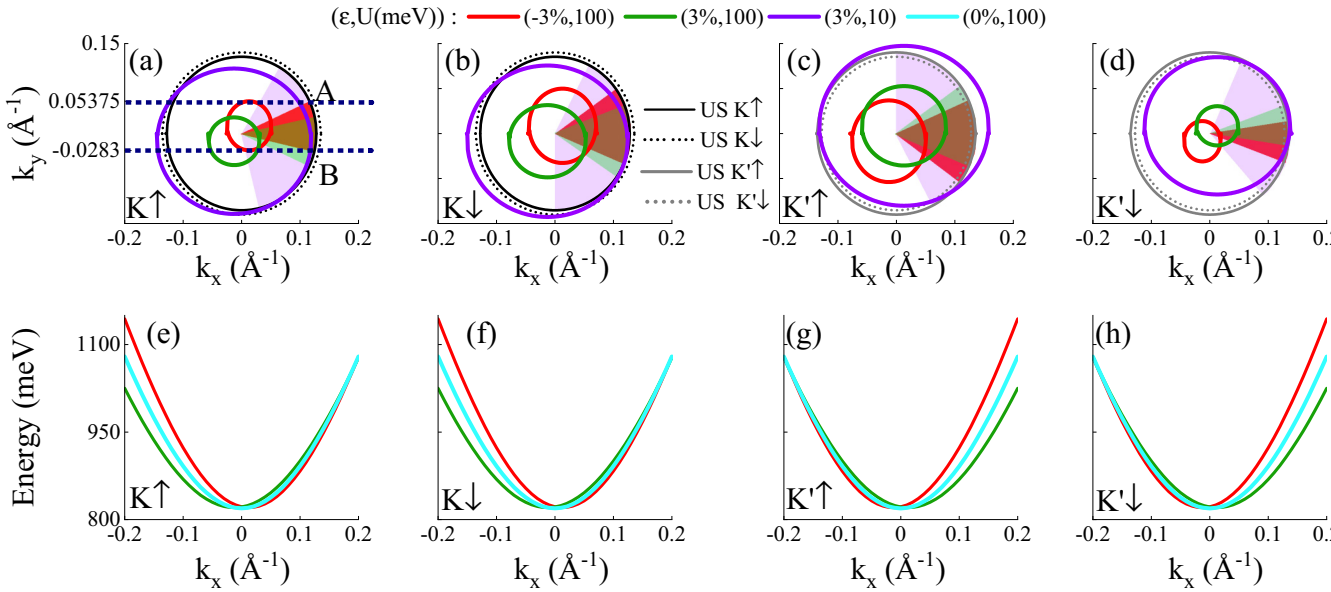

FIG. 3. (a)–(d) Isoenergy surfaces (ISs) of the strained (colored circles) and the unstrained (US) regions (black circles for the K valley and gray ones for the K' valley) under various configurations of $(\epsilon, U(\text{meV}))$. The colored shaded parts represent the range of allowed angles in which significant transmission may occur. (e)–(h) Band structures under different ϵ with $U = 100$ meV. The coordinates of point A are $(0.116, 0.053\,75)$ Å^{-1}, and those of point B are $(0.125, -0.0283)$ Å^{-1}. The parameters are $B_c = 10$ meV, $B_v = 8$ meV, $\lambda_R = 2$ meV, and $\theta = 0.25\pi$.

spin and valley indexes. One can see that the Dirac point is shifted compared with the unstrained one, thus generating a pseudovector potential induced by strain. Take the K valley as an example [see Figs. 3(e) and 3(f)]; when $\epsilon = 0$, we find that the Dirac point is given at $k_x = 0$. When $\epsilon = 3\%$ and $\theta = 0.25\pi$, the Dirac point shifts to $k_x = -0.01$ Å^{-1}, whereas the Dirac point shifts to $k_x = 0.01$ Å^{-1} when $\epsilon = -3\%$. Figures 3(g) and 3(h) show that the displacement direction of the Dirac point under strain in the K' valley is opposite in the K valley, which can be explained by the pseudovector potential $\mathbf{q}_D$.

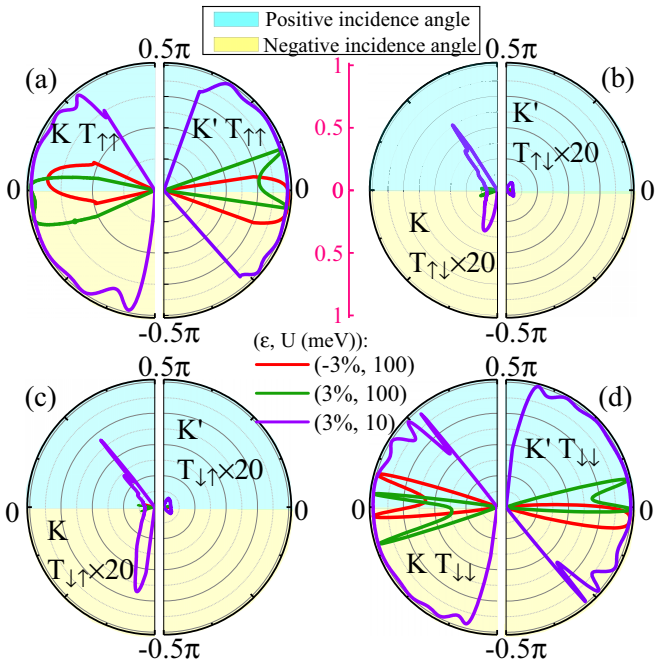

FIG. 4. (a)–(d) Angular distributions of $T_{ss'}$ in the two valleys with different configurations of $(\epsilon, U(\text{meV}))$. The incident energy is $E = 950$ meV, $B_c = 10$ meV, $B_v = 8$ meV, $\lambda_R = 2$ meV, $L = 10$ nm, and $\theta = 0.25\pi$.

In Fig. 4, we display the valley- and spin-dependent transmission probabilities without ($T_{\uparrow\uparrow}$ and $T_{\downarrow\downarrow}$) and with spin flip ($T_{\uparrow\downarrow}$ and $T_{\downarrow\uparrow}$) as a function of the incident angle with various combinations of $(\epsilon, U(\text{meV}))$. It is seen that the spin-flipped scattering is finite because the effect of the Rashba spin-orbit coupling (SOC) is considered [see Figs. 4(b) and 4(c)]. In the presence of the strain modulus ϵ, both the spin-conserved and spin-flipped transmissions show asymmetric angular distributions about $\phi = 0$. As ϵ increases, the transmission spectra show distinct valley-dependent transport behaviors. That is, for the K valley, the region of incident angle that can transmit the strained segment is reduced when $\phi \subset [0, \pi/2]$ and increases when $\phi \subset [-\pi/2, 0]$ [see Fig. 4(a)], while the region for the K' valley gets wider when $\phi \subset [0, \pi/2]$ and gets narrower when $\phi \subset [-\pi/2, 0]$ [see Fig. 4(d)]. Thus the difference in the angular distribution of transmission between the K and K' valleys can be effectively controlled via the strain. The physical mechanism of this valley filtering effect can be explained by the ISs, indicated by the shaded areas in Fig. 3, which are determined by the conservation of energy and momentum.

With decreasing applied voltage, it is observed that the allowed sectors are significantly broadened and dependent on the valley index. Furthermore, compared with (3%, 100), the transmission spectra at (3%, 10) show the effect of remarkable resonant enhancement [see Figs. 4(a) and 4(d)]. Moreover, it is evident that the allowed range for the transparent state with spin up is misaligned with the spin-down one. Therefore, since

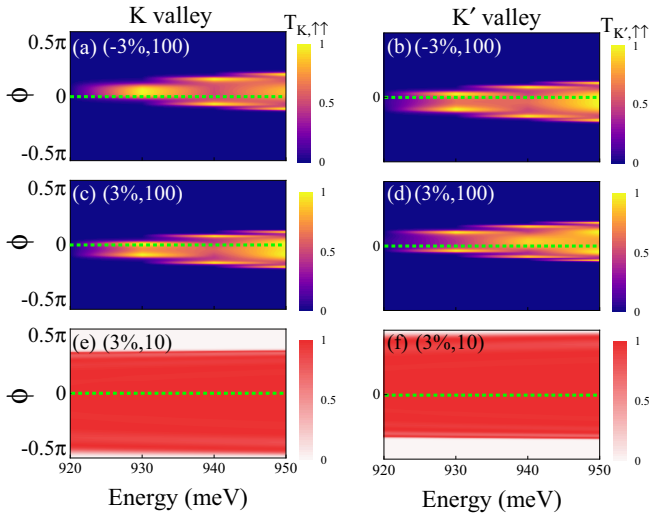

FIG. 5. $T_{\uparrow\uparrow}$ as a function of the incident angle ϕ and the incident energy for different configurations of $(\epsilon, U(\text{meV}))$ in the K valley [(a), (c), and (e)] and K' valley [(b), (d), and (f)]. $B_c = 10$ meV, $B_v = 8$ meV, $\lambda_R = 2$ meV, $L = 10$ nm, and $\theta = 0.25\pi$.

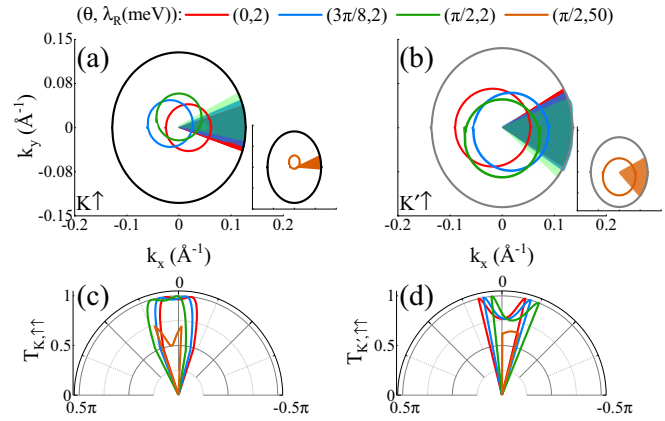

FIG. 6. (a) and (b) Isoenergy surfaces in the strained (colored circles) and the unstrained (black and gray circles) regions under different configurations of $(\theta, \lambda_R(\text{meV}))$ in the K and K' valleys with spin up, respectively. The shaded regions represent the range of incident angles in which transmission can occur. (c) and (d) Angular distributions of $T_{\uparrow\uparrow}$ under various $(\theta, \lambda_R(\text{meV}))$ in the K and K' valleys, respectively. The incident energy is $E = 950$ meV, $B_c = 10$ meV, $B_v = 8$ meV, $U = 100$ meV, and $\epsilon = 3\%$.

the transmission of spin- and valley-related particles depends on ϵ and U, the heterostructure with a suitable combination of $(\epsilon, U(\text{meV}))$ can be used as the spin valve and valley valve to filter the incoming beam at the same time.

$T_{\uparrow\uparrow}$ as a function of ϕ and incident energy with various combinations of $(\epsilon, U(\text{meV}))$ in the K valley is plotted in Figs. 5(a), 5(c), and 5(e), and that in the K' valley is plotted in Figs. 5(b), 5(d), and 5(f). In the presence of ϵ, $T_{\uparrow\uparrow}$ reveals asymmetric behavior about $\phi = 0$. Comparing Figs. 5(a) and 5(b), one can see that the degree of asymmetric behavior about $\phi = 0$ is significantly controlled by ϵ. When $U = 100$ meV, $T_{\uparrow\uparrow}$ under strains of both -3 and 3% is blocked within a broad angular range, as shown in Figs. 5(a)–5(d). However, the suppressed area becomes quite small when $U = 10$ meV [see Figs. 5(e) and 5(f)]. Note that the spectrum of the K valley is misaligned with that of the K' valley, i.e., the degeneracy of the valley is removed. Therefore one can expect that the strained MoS_2/EuO heterostructure can give rise to a valley filter effect.

In Fig. 6, we exhibit the valley-related ISs with spin-up state and $T_{K(K'),\uparrow\uparrow}$ under different configurations of $(\theta, \lambda_R(\text{meV}))$. From Figs. 6(a) and 6(b), it can be seen that with the changing of θ, the radius of the IS is unchanged, and the range of the allowed angles is unchanged. Apparently, the radius of the IS is caused by the elliptic equation $\epsilon_x{}^2 q_x{}^2 + \epsilon_y{}^2 q_y{}^2 = K^2$ according to Eq. (A4), and the two axes of the IS have lengths $2|K/\epsilon_x|$ and $2|K/\epsilon_y|$, respectively, which are independent of θ. Besides, the strained IS for the K (K') valley moves in the direction of positive (negative) incidence angle around the center of the unstrained IS with increasing θ. The equation of the ellipse shows that the center of the IS is (q_D, q_{Dy}) in phase space, which indicates that θ has an effect on the threshold of the allowed angles. Moreover, with increasing λ_R, the reduced radius of the IS results in the reduced range of allowed angles at both valleys [see the insets in Figs. 6(a) and 6(b)]. This can be understood with the help of the elliptic equation since increasing λ_R causes $|K|$ to decrease.

Next, we present $T_{K(K'),\uparrow\uparrow}$ versus the incident angle ϕ under different configurations of $(\theta, \lambda_R(\text{meV}))$. The following can be seen from Figs. 6(c) and 6(d): (1) Increasing θ does not affect the transport characteristics, but makes the sector of allowed angles for the K (K') valley move towards the region of positive (negative) incidence angle. (2) Increasing λ_R can suppress tunneling and narrow the range of allowed angles for both valleys. These phenomena can be explained by the overlap of ISs between the unstrained region and the strained region under the premise of k_y conservation, as depicted in Figs. 6(a) and 6(b). When $\lambda_R = 2$ meV, the IS in the unstrained segment overlaps well with that in the strained one. Therefore the transmission is significant. Increasing λ_R reduces the radius of the IS in the strained region, resulting in a reduction of the overlap with the unstrained one. Consequently, the transmission is suppressed dramatically, and the range of the allowed angles decreases.

In Fig. 7, $T_{K(K'),\uparrow\uparrow}$ are plotted as a function of the incident angle ϕ and the incident energy. When λ_R and ϵ are fixed, i.e., $\lambda_R = 2$ meV and $\epsilon = 3\%$, the overall section of the allowed angles for the K (K') valley moves towards the region of positive (negative) incidence angle, but the shape remains the same when θ is changed from 0π to $\pi/2$, as shown in Figs. 7(a)–7(d). When $\lambda_R = 50$ meV is considered [see Figs. 7(e) and 7(f)], it is found that increasing λ_R can reduce the range of the allowed angles and suppress the transmission probability. Another prominent feature of increasing θ is to amplify the asymmetry of transmission between the two valleys; that is, enhanced valley polarization appears when θ is increased. This enhanced effect is further demonstrated in Fig. 8, which displays the valley polarization of the incident particles with spin up and without spin flip and is determined by $P_V^{\uparrow\uparrow} = (T_{K,\uparrow\uparrow} - T_{K',\uparrow\uparrow})/(T_{K,\uparrow\uparrow} + T_{K',\uparrow\uparrow})$. Our study suggests the possibility of addressing a specific valley

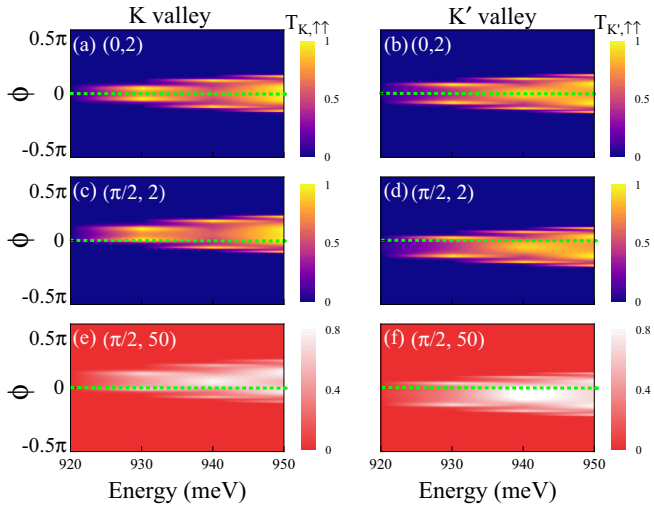

FIG. 7. $T_{\uparrow\uparrow}$ as a function of the incident angle ϕ and the incident energy under different configurations of $(\theta, \lambda_R(\text{meV}))$ in the K valley [(a), (c), and (e)] and K' valley [(b), (d), and (f)]. $B_c = 10$ meV, $B_v = 8$ meV, $U = 100$ meV, $\epsilon = 3\%$, and $L = 10$ nm.

by controlling the incident angle and the incident energy. On the other hand, the valley polarization can also be enhanced by regulating θ.

IV. SPIN POLARIZATION VECTOR

Figures 9 and 10 plot the components of the spin polarization vector as a function of the Fermi energy under different ϵ for $\lambda_R = 2$ meV [Figs. 9(a), 9(c), and 9(e) and Figs. 10(a), 10(c), and 10(e)] and $\lambda_R = 50$ meV [Figs. 9(b), 9(d), and 9(f) and Figs. 10(b), 10(d), and 10(f)]. Combining Fig. 9 when $\theta = 0$ and Fig. 10 when $\theta = 0.25\pi$, we can draw the following conclusions. (1) The spin-flipped scattering generated by Rashba SOC leads to the in-plane spin polarizations, i.e., P_X and P_Y, as shown in Figs. 9(a)–9(d) and Figs. 10(a)–10(d). (2) When ϵ is fixed, the components of the spin polarization oscillate with the Fermi energy. (3) The valleys and peaks of the in-plane spin polarization components P_X and P_Y move to the lower-energy region with the increase of ϵ. (4) Increasing ϵ significantly enhances the strengths of P_X and P_Y, and this tendency is not affected by λ_R. (5) The strength of P_Z depends on the competition between ϵ and λ_R. When λ_R is small, i.e., $\lambda_R = 2$ meV, the increase of ϵ increases the amplitude of P_Z;

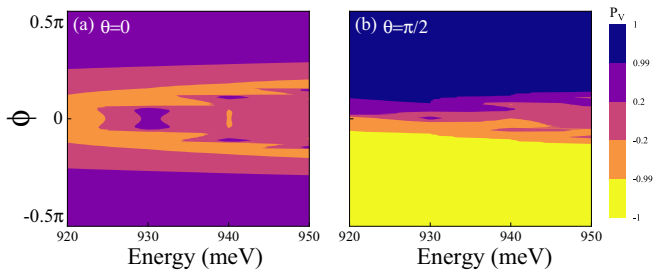

FIG. 8. Valley polarization as a function of the incident angle ϕ and the incident energy for (a) $\theta = 0$ and (b) $\theta = \pi/2$. $B_c = 10$ meV, $B_v = 8$ meV, $\lambda_R = 2$ meV, $\epsilon = 3\%$, and $L = 10$ nm.

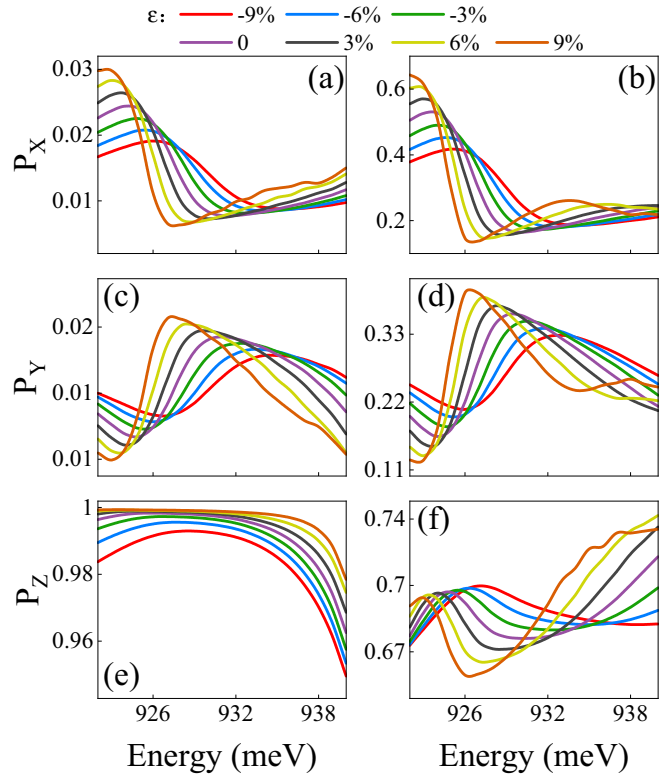

FIG. 9. The components of the spin polarization vector with variable ϵ. $B_c = 10$ meV, $B_v = 8$ meV, $\theta = 0$, and $U = 100$ meV. $\lambda_R = 2$ meV for (a), (c), and (e), and $\lambda_R = 50$ meV for (b), (d), and (f).

especially, when $\epsilon = 9\%$, P_Z approaches to 1 [see Figs. 9(e) and 10(e)]. When λ_R becomes larger, i.e., $\lambda_R = 50$ meV, we can see that the amplitude of P_Z decreases with the increase of ϵ [see Figs. 9(f) and 10(f)]. (6) Increasing λ_R enhances P_X and P_Y but suppresses P_Z. (7) The three components of the spin polarization vector change slightly with θ.

In order to better understand the regulation of strain on spin polarizations, we show the three components of the spin polarization vector as a function of ϵ at fixed Fermi energy $E_F = 932$ meV in Fig. 11. With increasing ϵ, both P_X and P_Y show oscillatory behaviors. One can observe that, for ϵ in the range $-20\% \leqslant \epsilon \leqslant 1\%$ and $\lambda_R = 2$ meV, P_X decreases distinctly with the increase in ϵ and closes to its minimum at 1%. When $1\% < \epsilon \leqslant 14.5\%$, P_X increases, and then it decreases when $\epsilon > 14.5\%$. Besides, the variation of P_Y with ϵ is just opposite to that of P_X, which is determined by the conservation of $|\mathbf{P}|$ [see Fig. 11(a)]. For the case of $\lambda_R = 50$ meV [see Fig. 11(b)], it is interesting that the extreme values of P_X and P_Y can be enhanced to 2.85 times and 34 times the corresponding values when $\lambda_R = 2$ meV, respectively.

Figures 11(c) and 11(d) clearly show that the strain can be used to modulate and magnify the magnitude of P_Z, in which P_Z can reach 100% at $\epsilon = 20\%$ when $\lambda_R = 2$ meV. We also find that, for relatively small λ_R, i.e., $\lambda_R = 2$ meV, P_Z increases continuously with ϵ [see Fig. 11(c)]. However, when $\lambda_R = 50$ meV, P_Z is suppressed and shows fluctuation with the increase in ϵ. From the evolution of P_X, P_Y, and P_Z with ϵ, we can arrive at the conclusion that strain is an effective means to

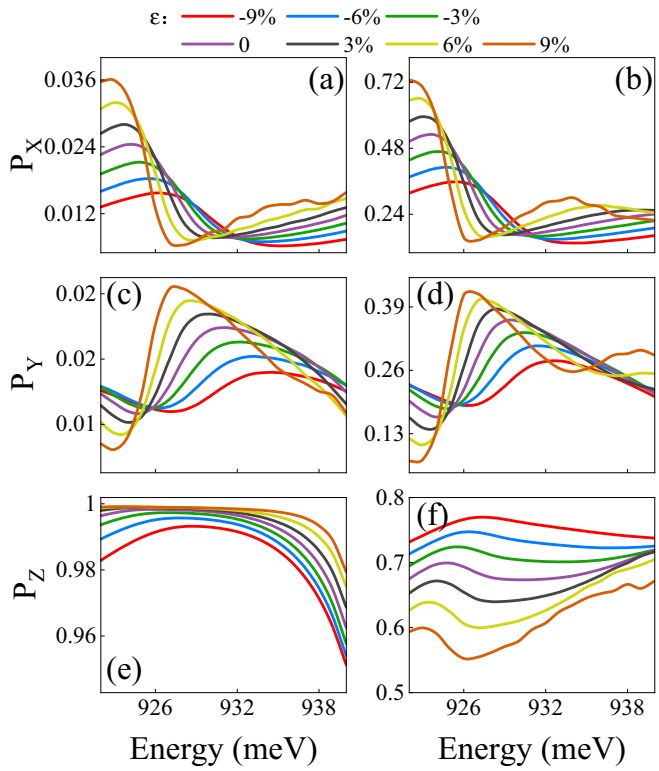

FIG. 10. The components of the spin polarization vector with variable ϵ. $B_c = 10$ meV, $B_v = 8$ meV, $\theta = 0.25\pi$, and $U = 100$ meV. $\lambda_R = 2$ meV for (a), (c), and (e), and $\lambda_R = 50$ meV for (b), (d), and (f).

adjust the strength of the spin polarizations and that the magnitude of P_X, P_Y, and P_Z is also sensitive to the Rashba field.

Further understanding of ϵ-modulated spin polarizations can be gained through Fig. 12, where G_{xy} and G_{ss} are plotted as a function of ϵ. When ϵ varies from -20 to 20%, Re$[G_{xy}]$ under both $\lambda_R = 2$ meV and $\lambda_R = 50$ meV mainly under-

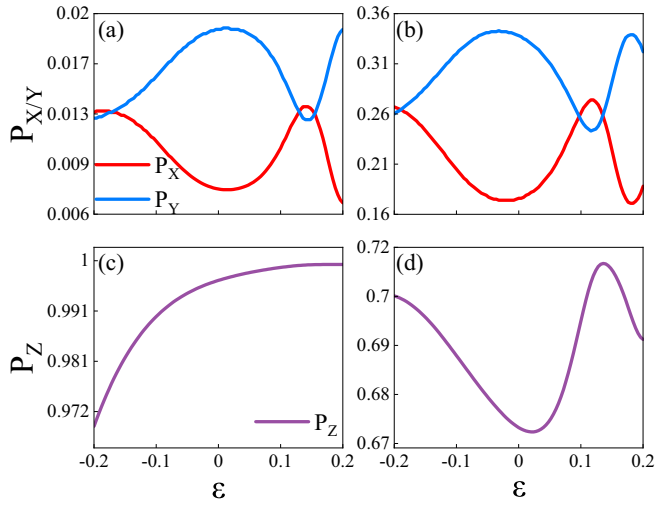

FIG. 11. The components of the spin polarization vector as a function of ϵ. $B_c = 10$ meV, $B_v = 8$ meV, $\theta = 0$, $E_F = 932$ meV, and $U = 100$ meV. $\lambda_R = 2$ meV for (a) and (c), and $\lambda_R = 50$ meV for (b) and (d).

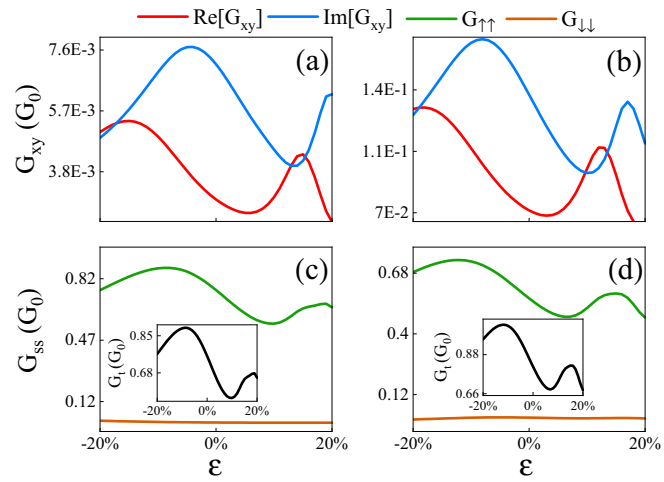

FIG. 12. (a) and (b) G_{xy} and (c) and (d) G_{ss} as a function of ϵ. $B_c = 10$ meV, $B_v = 8$ meV, $\theta = 0$, $E_F = 932$ meV, and $U = 100$ meV. The insets in (c) and (d) are the total conductance vs ϵ. $\lambda_R = 2$ meV for (a) and (c), and $\lambda_R = 50$ meV for (b) and (d).

goes the process of first decreasing, then increasing, and then decreasing [see Figs. 12(a) and 12(b)]. Correspondingly, the magnitude of P_X is oscillatory with ϵ according to Eq. (A8). In contrast, the fluctuating behavior of Im$[G_{xy}]$ is the opposite of Re$[G_{xy}]$, which leads to the corresponding change in P_Y. In addition, the magnitude of both Re$[G_{xy}]$ and Im$[G_{xy}]$ is enhanced when λ_R increases from 2 to 50 meV. Consequently, P_X and P_Y are enlarged when $\lambda_R = 50$ meV. $G_{\uparrow\uparrow}$ and $G_{\downarrow\downarrow}$ are plotted in Figs. 12(c) and 12(d). It is clearly shown that $G_{\uparrow\uparrow}$ possesses obvious value, while $G_{\downarrow\downarrow}$ is greatly suppressed. Accordingly, the magnitude of P_Z is quite large. We also find that the decreasing trend of $G_{\uparrow\uparrow}$ when $-8\% \leqslant \epsilon \leqslant 10\%$ and $\lambda_R = 2$ meV is canceled out by the more rapid decrease of G_t [see inset in Fig. 12(c)], resulting in the increase of P_Z with ϵ. However, the more pronounced reduction in $G_{\uparrow\uparrow}$ when $-12\% \leqslant \epsilon \leqslant 7\%$ and $\lambda_R = 50$ meV cannot be eliminated by the drop in G_t [see inset in Fig. 12(d)], causing P_Z to oscillate with ϵ.

V. OPTICAL CONDUCTIVITY

To demonstrate how the longitudinal and transverse optical conductivities are modified by strain, we employ the Kubo-Greenwood formula within the linear response theory and in the optical limit, and a derivation of the strained optical conductivity is given in Appendix B. Figure 13 represents the real part of the transverse conductivities Re σ_{xy} and the longitudinal conductivities Re σ_{xx} as a function of radiation frequency f without and with strain at various Fermi energies. The spin splitting of the conduction band in the TMD system is up to 72 meV induced by the proximity, which is less than the band gap and within the terahertz regime. Therefore the analysis only focus on the VHE contributed by the spin-flip interband transition of electrons within the conduction band. In addition, for ML MoS_2, the Fermi energy can be tuned by the gate voltage. As can be seen from Fig. 13, for a specific E_F, the position of the absorption peak or valley and the width of the absorption window are slightly affected by

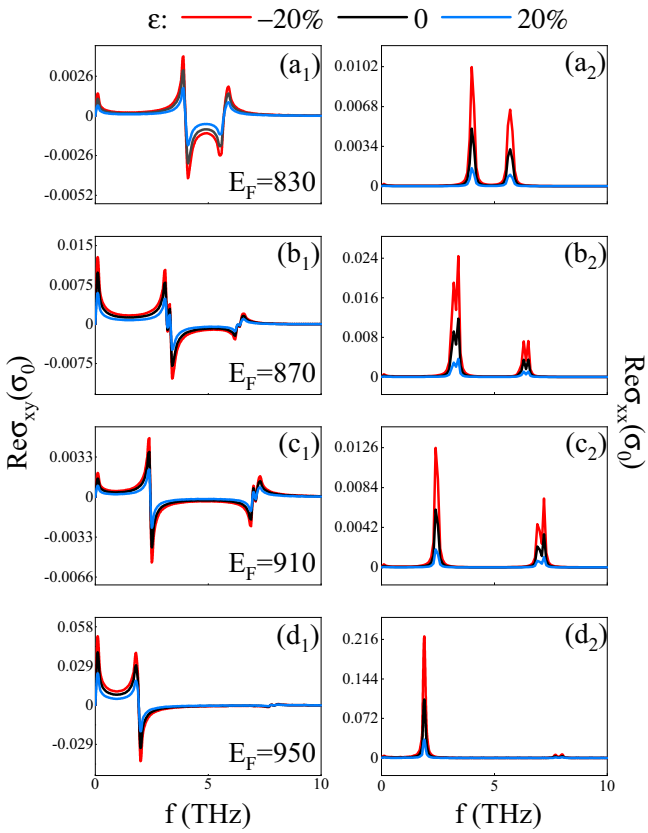

FIG. 13. Real parts of the optical conductivities as a function of radiation frequency under variable ϵ. (a1) and (a2) $E_F = 830$ meV, (b1) and (b2) $E_F = 870$ meV, (c1) and (c2) $E_F = 910$ meV, and (d1) and (d2) $E_F = 950$ meV. $B_c = 10$ meV, $B_v = 8$ meV, $\lambda_R = 2$ meV, and $T = 5$ K.

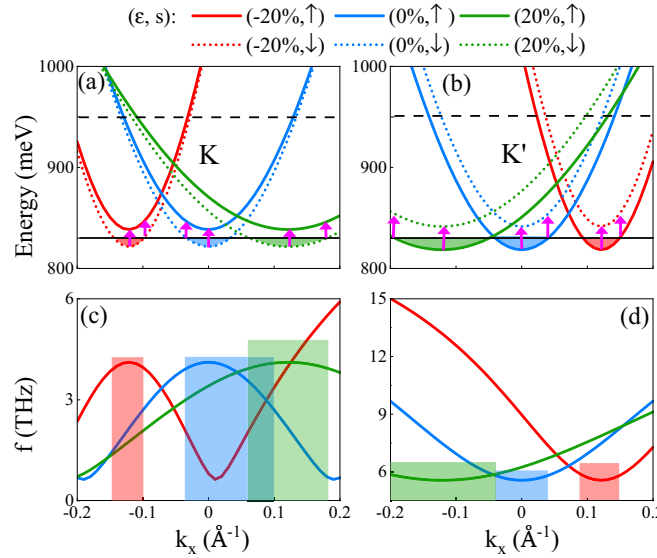

FIG. 14. (a) and (b) Band structures of the conduction band and possible transition channels under different strain moduli. The solid and dotted colored lines indicate the spin-up and spin-down subbands, respectively. The solid and dashed black lines are the positions of $E_F = 830$ meV and $E_F = 950$ meV, respectively. (c) and (d) Radiation frequency range within which excitation of the spin-flip interband transition is possible when $E_F = 830$ meV; the shaded areas indicate the range of wave vectors k_x and the corresponding frequency interval where the transition can occur. For the red shading, $\epsilon = -20\%$; for the blue shading, $\epsilon = 0\%$; and for the green shading, $\epsilon = 20\%$. $B_v = 10$ meV, $B_c = 8$ meV, $\lambda_R = 2$ meV, and $T = 5$ K. (a) and (b) are for the K valley, and (b) and (d) are for the K' valley.

strain. Nevertheless, it is interesting that the amplitudes of both the absorption peak and the absorption valley are reduced when ϵ changes from -20 to 20%. Apart from the effect of strain on the window of optical transition, the intensity of the absorption peak or valley and the position and the width of the absorption window are also obviously affected by the Fermi energy. As shown in Fig. 13, we find that the first absorption peak and valley shift to the lower frequency, whereas the second absorption peak and valley shift to the higher frequency with increasing E_F.

The Fermi energy and the strain-tuned band structure determine the possible interband spin-flip optical transition channels and then characterize the features of the absorption window. To reveal the response mechanism of the Hall conductivity to terahertz frequency under the application of strain, we plot the band structure under variable strain, with $E_F = 830$ meV falling between the two spin-split conduction bands and $E_F = 950$ meV falling above the higher conduction band. As can be seen in Figs. 14(a) and 14(b), the splitting of subbands in K and K' is asymmetric; that is, the spin-up subband is above the spin-down one for the K valley, while this splitting behavior is reversed for the K' valley. The inequivalent spin-splitting behavior between the two valleys and the distinct difference of the spin splitting between the subbands in a certain valley lead to the observable VHE within the terahertz frequency. Moreover, it can be proved from Eq. (B1) that the interaction matrix element decreases as ϵ increases. Therefore such a feature leads to the suppression effect of increasing ϵ on the absorption peak and valley. Besides, we find that the strained Dirac points on the two valleys shift in opposite directions relative to the unstrained Dirac point. The strain-modulated energy difference between spin-splitting subbands in a specific valley and the valley-related displacement of the Dirac point under strain affect the absorption windows of optical conductivities. Moreover, varying the Fermi energy results in the change of the transition channel and the shift of the absorption window. For example, when $E_F = 830$ meV and $\epsilon = -20\%$ [see Figs. 14(c) and 14(d)], the range of the wave vectors wherein the optical transition from the lower occupied state to the higher empty state may occur is about -0.14 to -0.09 Å^{-1} for the K valley, and it is about 0.088–0.15 Å^{-1} for the K' valley. As a result, the absorption window of the transition within the K valley is around 4 THz [the first absorption peak in Fig. 13(a1)], while it is around 6 THz in the K' valley [the second absorption peak in Fig. 13(a1)]. For the case of $E_F = 950$ meV, the transition window corresponding to the K valley is around 2 THz [the first absorption peak in Fig. 13(d1)], whereas the window in the K' valley is around 8 THz [the second absorption peak in Fig. 13(d1)].

Next, we characterize the dependence of the Hall conductivity on the Rashba parameter λ_R and temperature. In Fig. 15,

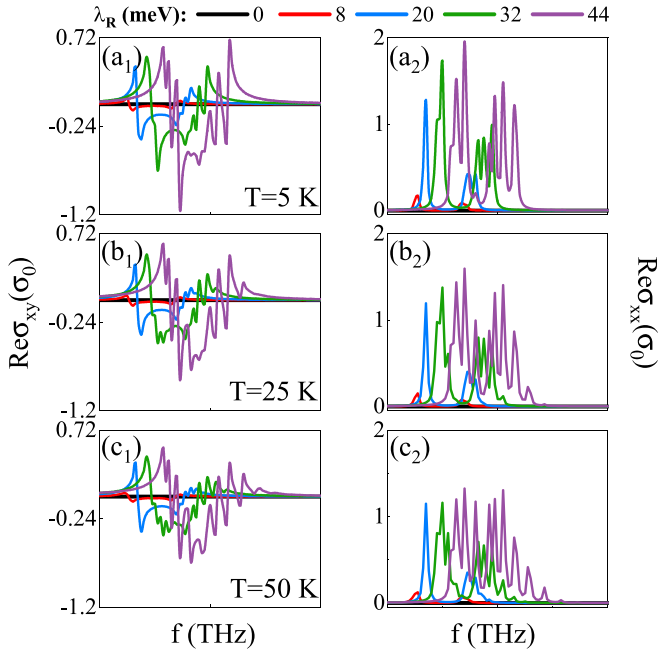

FIG. 15. Real parts of the optical conductivities as a function of radiation frequency with variable λ_R. (a1) and (a2) $T = 5$ K, (b1) and (b2) $T = 25$ K, and (c1) and (c2) $T = 50$ K. $B_c = 10$ meV, $B_v = 8$ meV, $\epsilon = -20\%$, and $E_F = 830$ meV.

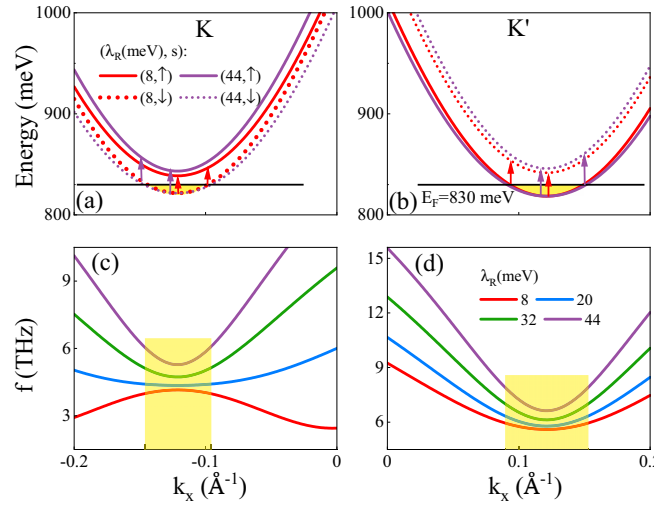

FIG. 16. (a) and (b) Band structures of conduction band and possible transition channels under different λ_R. The solid and dotted colored lines indicate the spin-up and spin-down subbands, respectively. The solid black line is the position of $E_F = 830$ meV. (c) and (d) Radiation frequency range within which excitation of the spin-flip interband transition is possible; the yellow shaded area indicates the range of wave vectors k_x and the corresponding frequency interval where the transition can occur when $E_F = 830$ meV. $B_c = 10$ meV, $B_v = 8$ meV, and $\epsilon = -20\%$. (a) and (c) are for the K valley, and (b) and (d) are for the K' valley.

we show Reσ_{xy} [Figs. 15(a1), 15(b1), and 15(c1)] and Reσ_{xx} [Figs. 15(a2), 15(b2), and 15(c2)] as a function of the radiation frequency under several combinations of (λ_R(meV), T). It is observed that the value of Reσ_{xy} is almost zero and is independent of temperature when λ_R is not considered. With increasing λ_R, the positions of peak and valley move to the higher-frequency region. Furthermore, we find that increasing λ_R not only can strengthen the absolute values of both peaks and valleys, but also can increase the numbers of peaks and valleys. Our study illustrates that λ_R has the effect of exciting the generation of optical Hall conductivity within the terahertz frequency and adjusting the response of the Hall conductivity to the frequency. Besides varying λ_R, the profile of optical conductivity can also be modulated by the temperature. As shown in Fig. 15, we find a strong T dependence. As the temperature T increases from 5 to 50 K, the magnitudes of both the absorption peaks and the absorption valleys are significantly weakened.

Plots of the band structures and the ranges of radiation frequency in which the spin-flip interband transition within the conduction band occurs for several values of λ_R are shown in Fig. 16. With the enhancement of λ_R, the upper spin subband moves upward, whereas the lower spin subband changes slightly, which leads to the increase in the energy difference between the two spin subbands in the specific valley and the shift of the absorption window to the higher-frequency region [see Figs. 16(c) and 16(d)]. Note that there are more channels transiting from the lower occupied state to the higher empty state when λ_R increases, which gives the features of the rise in the magnitude of the absorption peak and the broadening of the absorption window.

VI. CONCLUSIONS

In this paper, we theoretically studied spin- and valley-dependent transmission and valley Hall conductivity in the strained n-type MoS_2/EuS heterostructure under linearly polarized terahertz radiation. We mainly investigated how strain intensity ϵ, strain direction θ, and Rashba coupling parameter λ_R regulate the threshold and range of allowed angles, spin polarization components, and optical conductivity. The main conclusions are summarized as follows.

(1) Due to the presence of λ_R, there appear spin and valley splittings simultaneously in the n-type MoS_2/EuS heterostructure. Thus we find that the displacement of the Dirac point induced by the strain becomes valley dependent, and the band edge energy oscillates as a function of ϵ and θ. Interestingly, it is found that ϵ can tune the threshold and range of allowed angles and transmission probability, while θ only affects the former.

(2) Owing to the spin-flipped scattering generated by Rashba spin-orbit coupling, in-plane spin polarizations, i.e., P_X and P_Y, can be achieved. We demonstrate that the strength of P_X and P_Y can be distinctly enhanced by varying ϵ but is only slightly affected by θ, which is due to the effect of strain on the spin-dependent transmission. It is worth emphasizing that P_Z is subject to the complicated competition between λ_R and ϵ. For the case of a smaller λ_R, i.e., $\lambda_R = 2$ meV, P_Z increases monotonically as a function of ϵ. Nevertheless, when λ_R is larger, i.e., $\lambda_R = 50$ meV, P_Z shows oscillatory behavior with increasing ϵ.

(3) The optical conductivity can be obtained in our proposed heterostructure in the presence of linearly polarized

terahertz radiation. It is demonstrated that by changing ϵ we can tune the magnitude of both the absorption peaks and the absorption valleys in optical conductivity, which originates from the modulation, by strain, of the band structure and band edge energy. Furthermore, the absorption window of optical conductivity can also be modulated by varying λ_R.

Our work demonstrates that the strain is an effective means of tuning the transport characteristics without and with spin flip and the strength of spin polarizations. It is found that the regulation and enhancement of optical conductivity in the terahertz frequency region can be achieved by applying strain. Our results provide a possibility to use elastic strain to improve and control the optical Hall effect through terahertz technology in *n*-type MoS_2-based heterostructures.

ACKNOWLEDGMENTS

This work was supported by the National Natural Science Foundation of China under Grant No. 12074209.

APPENDIX A: DERIVATION OF THE TRANSMISSION PROBABILITY

In this Appendix, we start by considering the solution of the Dirac equation of the unstrained region $U^\dagger(\theta)\Psi_I^{\uparrow(\downarrow)}(x)e^{ik_y y}$ for the electron with incident energy E_0 and incident angle ϕ, in which $\Psi_I^{\uparrow(\downarrow)}(x)$ can be expressed as

$$\Psi_I^{\uparrow(\downarrow)}(x) = \mathcal{A}^{\uparrow(\downarrow)}(1(0),\ 0(1),\ a_\pm(0),\ 0(\mathcal{b}_\pm))^T e^{\pm ik_x^{\uparrow(\downarrow)}x}, \tag{A1}$$

where

$$\begin{aligned}
a_\pm &= at(\mp\tau k_x^\uparrow - ik_y^\uparrow)/d_2,\\
\mathcal{b}_\pm &= at(\mp\tau k_x^\downarrow - ik_y^\downarrow)/d_3,\\
\mathcal{A}^{\uparrow(\downarrow)} &= (1 + a(\mathcal{b})_+^2)^{-1/2},\\
d_{0(1)} &= \Delta/2 \pm \tau\lambda_c - E_0,\\
d_{2(3)} &= -\Delta/2 \pm \tau\lambda_v - E_0,\\
k_x^{\uparrow(\downarrow)} &= \sqrt{(d_0d_2 + d_1d_3 \mp (d_1d_3 - d_0d_2))/2}\cos\phi,\\
k_y^{\uparrow(\downarrow)} &= \sqrt{(d_0d_2 + d_1d_3 \mp (d_1d_3 - d_0d_2))/2}\sin\phi.
\end{aligned} \tag{A2}$$

The wave function in the strained region can be written as $U^\dagger(\theta)\Psi_{II}(x)e^{ik_y y}$, with

$$\Psi_{II}(x) = \mathcal{B}\big(e_\pm,\quad j,\quad 1,\quad g_\pm\big)^T e^{\pm i(q_x \pm q_D)x}, \tag{A3}$$

where

$$\begin{aligned}
e_\pm &= \mp at(\tau\epsilon_x q_x \mp i\epsilon_y q_y)/h_0,\\
j &= \big[-a^2t^2\big(\epsilon_x^2q_x^2 + \epsilon_y^2q_y^2\big) + h_0h_2\big]/2i\lambda_R h_0,\\
g_\pm &= [\mp atf(\tau\epsilon_x q_x \pm i\epsilon_y q_y)]/h_3,\\
\mathcal{B} &= (e_+^2 + f^2 + 1 + g_+^2)^{-1/2},\\
h_{0(1)} &= \Delta/2 \pm h_\tau^c - E_0 + U,\\
h_{2(3)} &= -\Delta/2 \pm h_\tau^v - E_0 + U,\\
q_x &= \sqrt{\big(K^2 - \epsilon_y^2q_y^2\big)/\epsilon_x^2},\\
K &= \sqrt{\big(h_0h_2 + h_1h_3 - s\tau\sqrt{(h_0h_2 - h_1h_3)^2 + 16\lambda_R^2h_0h_3}\big)/2a^2t^2}.
\end{aligned} \tag{A4}$$

The conservation of the particle current ensures that $\langle J_x\rangle$ is constant, which can be derived from the current density operator $\mathbf{J} = -ie/\hbar[H, \mathbf{r}]$. In this case, the wave function at the interface satisfies the following relations:

$$\begin{aligned}
\Psi_{\rm I}(x=0) &= \epsilon_x^{-1/2}\Psi_{\rm II}(x=0),\\
\epsilon_x^{-1/2}\Psi_{\rm II}(x=L) &= \Psi_{\rm III}(x=L).
\end{aligned} \tag{A5}$$

Employing the above boundary conditions, we eventually arrive at the transmission probability, $T_{\tau,ss'} = |t_{\tau,ss'}|^2$, where $t_{\tau,ss'}$ represents the transmission coefficient for an incident electron with spin s in region I being transmitted into region III with spin s'. The eigenvalue of the strained Hamiltonian is given by

$$E^4 + \gamma_3E^3 + \gamma_2E^2 + \gamma_1E + \gamma_0 = 0, \tag{A6}$$

with

$$\begin{aligned}
\gamma_3 &= -4U,\\
\gamma_2 &= -2A^2\big(\epsilon_x^2q_x^2 + \epsilon_y^2q_y^2\big) - \Delta^2/2 - h_\tau^{c\,2} - h_\tau^{v\,2} - 4\lambda_R^2 + 6U^2,\\
\gamma_1 &= 4A^2U\big(\epsilon_x^2q_x^2 + \epsilon_y^2q_y^2\big)\\
&\quad + \big(h_\tau^c + h_\tau^v\big)\big(-\Delta h_\tau^c + \Delta h_\tau^v + 2Uh_\tau^c + 2Uh_\tau^v\big),\\
&\quad + 4U\big(\Delta^2/4 - h_\tau^ch_\tau^v - U^2\big) + 4\lambda_R^2\big(h_\tau^c - h_\tau^v + 2U\big),\\
\gamma_0 &= A^4\big(\epsilon_x^2q_x^2 + \epsilon_y^2q_y^2\big)^2\\
&\quad + A^2\big(\epsilon_x^2q_x^2 + \epsilon_y^2q_y^2\big)\big(\Delta^2/2 - 2h_\tau^ch_\tau^v - 2U^2\big)\\
&\quad + \big(-\Delta^2/4 + h_\tau^ch_\tau^v + U^2\big)^2\\
&\quad - \big(\Delta/2h_\tau^c - \Delta/2h_\tau^v - h_\tau^cU - h_\tau^vU\big)^2\\
&\quad - 4\lambda_R^2\big(\Delta/2 + h_\tau^c + U\big)\big(-\Delta/2 - h_\tau^v + U\big).
\end{aligned} \tag{A7}$$

The components of the spin polarization vector $\mathbf{P} = (P_X, P_Y, P_Z)$ are [55]

$$G_{ss'} = G_0 \sum_{\tau} \int_{-\pi/2}^{\pi/2} |t_{\tau,ss'}|^2 \cos\phi d\phi,$$
$$P_X = \mathrm{Re}\left[\frac{2G_{xy}}{G_t}\right],$$
$$P_Y = \mathrm{Im}\left[\frac{2G_{xy}}{G_t}\right],$$
$$P_Z = \frac{G_{\uparrow\uparrow} + G_{\downarrow\uparrow} - G_{\downarrow\downarrow} - G_{\uparrow\downarrow}}{G_t}, \tag{A8}$$

where $G_{xy} = G_0 \sum_{\tau,s} \int_{-\pi/2}^{\pi/2} t_{\tau,s\downarrow} t^*_{\tau,s\uparrow} \cos\phi d\phi$ and G_t is the total conductance

$$G_t = G_{\uparrow\uparrow} + G_{\downarrow\uparrow} + G_{\downarrow\downarrow} + G_{\uparrow\downarrow}. \tag{A9}$$

APPENDIX B: OPTICAL CONDUCTIVITY

In order to calculate the Hall conductance under the action of linearly polarized terahertz radiation, we follow the Kubo-Greenwood formula within the linear response theory [56]:

$$\sigma_{\mu\nu}(\omega) = \sigma^{\mathrm{dia}}_{\mu\nu} + \frac{ie^2}{\omega} \sum_{\beta\neq\beta'} \times \frac{\langle\beta|\upsilon_\mu|\beta'\rangle\langle\beta'|\upsilon_\nu|\beta\rangle[\mathbb{F}(E_\beta) - \mathbb{F}(E_{\beta'})]}{E_\beta - E_{\beta'} + \hbar(\omega + i\delta)}, \tag{B1}$$

where $\mu, \nu = x, y$, $\sigma^{\mathrm{dia}}_{\mu\nu} = \frac{-e^2 n_e}{i\omega m}\delta(\mathbf{k} - \mathbf{k}')\delta_{\mu\nu}$ is the diamagnetic term, $\beta = |\tau, s, \mathbf{k}\rangle$ is the single electron state when only the conduction is considered, $\upsilon_{\mu(\nu)} = \partial H/\partial p_{\mu(\nu)}$ is the component of group velocity, ω is the photon frequency, $\delta \to 0^+$, and $\mathbb{F}(E_\beta)$ is the Fermi-Dirac distribution. Notice that for intraband transition, $\mathbb{F}(E_\beta) - \mathbb{F}(E_{\beta'}) = 0$, which causes the transverse Hall conductivity to disappear. Therefore only the spin-flip interband transition within the conduction band is taken into account in the following discussion.

The velocity matrix elements are

$$\langle\beta'|\upsilon_x|\beta\rangle = \frac{\tau\mathcal{B}'\mathcal{B}A\epsilon_x}{\hbar}(e^{*\prime} + j^{*\prime}g + e + g^{*\prime}j),$$
$$\langle\beta'|\upsilon_y|\beta\rangle = \frac{i\mathcal{B}'\mathcal{B}A\epsilon_y}{\hbar}(-e^{*\prime} - j^{*\prime}g + e + g^{*\prime}j); \tag{B2}$$

thus

$$\langle\beta|\upsilon_x|\beta'\rangle\langle\beta'|\upsilon_x|\beta\rangle = \frac{\mathcal{B}'^2\mathcal{B}^2A^4\epsilon_x^2K^2}{\hbar^2}(\mathcal{P}^2 + \mathcal{W}^2 + 2\mathcal{P}\mathcal{W}\cos2\alpha)\delta_{\mathbf{k},\mathbf{k}'} \tag{B3}$$

and

$$\langle\beta|\upsilon_x|\beta'\rangle\langle\beta'|\upsilon_y|\beta\rangle = \frac{-i\tau\mathcal{B}'^2\mathcal{B}^2A^4\epsilon_x\epsilon_yK^2}{\hbar^2}\left(\mathcal{P}^2 - \mathcal{W}^2 + 2i\tau\mathcal{P}\mathcal{W}\sin2\alpha\right)\delta_{\mathbf{k},\mathbf{k}'}, \tag{B4}$$

with

$$\mathcal{P} = 1/h_0' + (-A^2K^2 + h_0h_2)(-A^2K^2 + h_0'h_2')/4\lambda_R^2h_0h_0'h_3,$$
$$\mathcal{W} = 1/h_0 + (-A^2K^2 + h_0h_2)(-A^2K^2 + h_0'h_2')/4\lambda_R^2h_0h_0'h_3'. \tag{B5}$$

Since the intervalley transition requires a considerable momentum transfer, which is impossible for direct electron-phonon interaction, the total optical conductivity can be regarded as the sum of the conductances of the two valleys:

$$\sigma_{\mu\nu}(\omega) = \sum_{\tau} \sigma^{\tau}_{\mu\nu}(\omega). \tag{B6}$$

When only the spin-flip transition between subbands in the conduction band is considered, the contributions of each valley to the longitudinal conductivity and transverse conductivity are

$$\sigma_{xx} = \sigma_0 \sum_{\tau} \int dK \frac{i\mathcal{B}'^2\mathcal{B}^2A^4\epsilon_x^2K^3(\mathcal{P}^2 + \mathcal{W}^2)}{\pi^2\hbar^2 f} \times \frac{\mathbb{F}\left(E_s^\tau\right) - \mathbb{F}\left(E_{s'}^\tau\right)}{\omega_{ss'} + \omega + i/\tau_s}, \tag{B7}$$

$$\sigma_{xy} = \sigma_0 \sum_{\tau} \int dK \frac{\tau\mathcal{B}'^2\mathcal{B}^2A^4\epsilon_x\epsilon_yK^3(\mathcal{P}^2 - \mathcal{W}^2)}{\pi^2\hbar^2 f} \times \frac{\mathbb{F}\left(E_s^\tau\right) - \mathbb{F}\left(E_{s'}^\tau\right)}{\omega_{ss'} + \omega + i/\tau_s}, \tag{B8}$$

where $\sigma_0 = e^2/4\hbar$, $f = \omega/2\pi$ is the radiation frequency, $\omega_{ss'} = (E_s - E_{s'})/\hbar$, and $\tau_s = 3$ ps is the spin relaxation time for electrons [57].

[1] Y. Ye, J. Xiao, H. Wang, Z. Ye, H. Zhu, M. Zhao, Y. Wang, J. Zhao, X. Yin, and X. Zhang, Nat. Nanotechnol. **11**, 598 (2016).

[2] X. D. Xu, W. Yao, D. Xiao, and T. F. Heinz, Nat. Phys. **10**, 343 (2014).

[3] Y. P. Liu, Y. J. Gao, S. Y. Zhang, J. He, J. Yu, and Z. W. Liu, Nano Res. **12**, 2695 (2019).

[4] J. R. Schaibley, H. Y. Yu, G. Clark, P. Rivera, J. S. Ross, K. L. Seyler, W. Yao, and X. D. Xu, Nat. Rev. Mater. **1**, 16055 (2016).

[5] G. B. Liu, W. Y. Shan, Y. G. Yao, W. Yao, and D. Xiao, Phys. Rev. B **88**, 085433 (2013).

[6] M. A. Cazalilla, H. Ochoa, and F. Guinea, Phys. Rev. Lett. **113**, 077201 (2014).

[7] W. Y. Shan, H. Z. Lu, and D. Xiao, Phys. Rev. B **88**, 125301 (2013).

[8] N. Ubrig, S. Jo, M. Philippi, D. Costanzo, H. Berger, A. B. Kuzmenko, and A. F. Morpurgo, Nano Lett. **17**, 5719 (2017).

[9] K. F. Mak, K. L. McGill, J. Park, and P. L. McEuen, Science **344**, 1489 (2014).

[10] W. X. Feng, Y. G. Yao, W. G. Zhu, J. J. Zhou, W. Yao, and D. Xiao, Phys. Rev. B **86**, 165108 (2012).

[11] G. Wang, C. Robert, M. M. Glazov, F. Cadiz, E. Courtade, T. Amand, D. Lagarde, T. Taniguchi, K. Watanabe, B. Urbaszek, and X. Marie, Phys. Rev. Lett. **119**, 047401 (2017).
[12] W. Yao, D. Xiao, and Q. Niu, Phys. Rev. B **77**, 235406 (2008).
[13] C. J. Ciccarino, T. Christensen, R. Sundararaman, and P. Narang, Nano Lett. **18**, 5709 (2018).
[14] X. N. Zhao, W. Xu, Y. M. Xiao, J. Liu, B. Van Duppen, and F. M. Peeters, Phys. Rev. B **101**, 245412 (2020).
[15] K. F. Mak, K. He, J. Shan, and T. F. Heinz, Nat. Nanotechnol. **7**, 494 (2012).
[16] T. Cao, G. Wang, W. P. Han, H. Q. Ye, C. R. Zhu, J. R. Shi, Q. Niu, P. H. Tan, E. G. Wang, B. L. Liu, and J. Feng, Nat. Commun. **3**, 887 (2012).
[17] D. N. Liu and Y. Guo, Appl. Phys. Lett. **118**, 123101 (2021).
[18] D. N. Liu and Y. Guo, Phys. Rev. B **106**, 035411 (2022).
[19] D. MacNeill, C. Heikes, K. F. Mak, Z. Anderson, A. Kormányos, V. Zólyomi, J. Park, and D. C. Ralph, Phys. Rev. Lett. **114**, 037401 (2015).
[20] R. Peng, Y. D. Ma, S. Zhang, B. Huang, and Y. Dai, J. Phys. Chem. Lett. **9**, 3612 (2018).
[21] C. Ke, Y. Wu, W. Yang, Z. Wu, C. Zhang, X. Li, and J. Kang, Phys. Rev. B **100**, 195435 (2019).
[22] G. Aivazian, Z. Gong, A. M. Jones, R. L. Chu, J. Yan, D. G. Mandrus, C. Zhang, D. Cobden, W. Yao, and X. Xu, Nat. Phys. **11**, 148 (2015).
[23] Y. F. Lin, C. C. Zhang, L. X. Guan, Z. P. Sun, and J. G. Tao, Nanomaterials **10**, 1642 (2020).
[24] B. Zhou, Z. Li, J. Wang, X. Niu, and C. Luan, Nanoscale **11**, 13567 (2019).
[25] T. Norden, C. Zhao, P. Zhang, R. Sabirianov, A. Petrou, and H. Zeng, Nat. Commun. **10**, 4163 (2019).
[26] C. Zhao, T. Norden, P. Zhang, P. Zhao, Y. Cheng, F. Sun, J. P. Parry, P. Taheri, J. Wang, Y. Yang, T. Scrace, K. F. Kang, S. Yang, G. X. Miao, R. Sabirianov, G. Kioseoglou, W. Huang, A. Petrou, and H. Zeng, Nat. Nanotechnol. **12**, 757 (2017).
[27] D. Zhong, K. L. Seyler, X. Linpeng, R. Cheng, N. Sivadas, B. Huang, E. Schmidgall, T. Taniguchi, K. Watanabe, M. A. McGuire, W. Yao, D. Xiao, K. M. C. Fu, and X. D. Xu, Sci. Adv. **3**, e1603113 (2017)..
[28] W. Z. Zhou, Z. X. Yang, A. L. Li, M. Q. Long, and F. P. Ouyang, Phys. Rev. B **101**, 045113 (2020).
[29] L. Xu, M. Yang, L. Shen, J. Zhou, T. Zhu, and Y. P. Feng, Phys. Rev. B **97**, 041405(R) (2018).
[30] Y. Song, X. C. Wang, and W. B. Mi, Adv. Electron. Mater. **3**, 1700245 (2017).
[31] Q. Y. Zhang, S. A. Yang, W. B. Mi, Y. C. Cheng, and U. Schwingenschlögl, Adv. Mater. **28**, 959 (2016).
[32] J. Qi, X. Li, Q. Niu, and J. Feng, Phys. Rev. B **92**, 121403(R) (2015).
[33] S. Y. Li, Y. Su, Y. N. Ren, and L. He, Phys. Rev. Lett. **124**, 106802 (2020).
[34] S. Bertolazzi, J. Brivio, and A. Kis, ACS Nano **5**, 9703 (2011).
[35] G. L. Yu, R. Jalil, B. Belle, A. S. Mayorov, P. Blake, F. Schedin, S. V. Morozov, L. A. Ponomarenko, F. Chiappini, S. Wiedmann, U. Zeitler, M. I. Katsnelson, A. K. Geim, K. S. Novoselov, and D. C. Elias, Proc. Natl. Acad. Sci. USA **110**, 3282 (2013).
[36] R. K. Defo, S. Fang, S. N. Shirodkar, G. A. Tritsaris, A. Dimoulas, and E. Kaxiras, Phys. Rev. B **94**, 155310 (2016).
[37] R. Schmidt, I. Niehues, R. Schneider, M. Drueppel, T. Deilmann, M. Rohlfing, S. M. De Vasconcellos, A. Castellanos-Gomez, and R. Bratschitsch, 2D Mater. **3**, 021011 (2016).
[38] D. Lloyd, X. Liu, J. W. Christopher, L. Cantley, A. Wadehra, B. L. Kim, B. B. Goldberg, A. K. Swan, and J. S. Bunch, Nano Lett. **16**, 5836 (2016).
[39] C. R. Zhu, G. Wang, B. L. Liu, X. Marie, X. F. Qiao, X. Zhang, X. X. Wu, H. Fan, P. H. Tan, T. Amand, and B. Urbaszek, Phys. Rev. B **88**, 121301(R) (2013).
[40] X. W. Zhao, Y. Li, R. D. Liang, G. C. Hu, X. B. Yuan, and J. F. Ren, Appl. Surf. Sci. **504**, 144367 (2020).
[41] M. Bilal, W. Xu, H. Wen, X. Cheng, Y. Xiao, and L. Ding, Opt. Lett. **46**, 2196 (2021).
[42] Z. Y. Zhu, Y. C. Cheng, and U. Schwingenschlögl, Phys. Rev. B **84**, 153402 (2011).
[43] H. Yuan, M. S. Bahramy, K. Morimoto, S. Wu, K. Nomura, B. Yang, H. Shimotani, R. Suzuki, M. Toh, C. Kloc, X. Xu, R. Arita, N. Nagaosa, and Y. Iwasa, Nat. Phys. **9**, 563 (2013).
[44] H. Min, J. E. Hill, N. A. Sinitsyn, B. R. Sahu, L. Kleinman, and A. H. MacDonald, Phys. Rev. B **74**, 165310 (2006).
[45] S. V. Eremeev, I. A. Nechaev, Y. M. Koroteev, P. M. Echenique, and E. V. Chulkov, Phys. Rev. Lett. **108**, 246802 (2012).
[46] A. O. Slobodeniuk and D. M. Basko, 2D Mater. **3**, 035009 (2016).
[47] A. Kormányos, V. Zólyomi, N. D. Drummond, and G. Burkard, Phys. Rev. X **4**, 011034 (2014).
[48] F. M. D. Pellegrino, G. G. N. Angilella, and R. Pucci, Phys. Rev. B **85**, 195409 (2012).
[49] M. Yarmohammadi, J. Magn. Magn. Mater. **426**, 621 (2017).
[50] V. M. Pereira, A. H. Castro Neto, and N. M. R. Peres, Phys. Rev. B **80**, 045401 (2009).
[51] M. Farokhnezhad, M. Esmaeilzadeh, and K. Shakouri, Phys. Rev. B **96**, 205416 (2017).
[52] S. Fang, S. Carr, M. A. Cazalilla, and E. Kaxiras, Phys. Rev. B **98**, 075106 (2018).
[53] D. W. Zhai and N. Sandler, Phys. Rev. B **98**, 165437 (2018).
[54] Y. J. Jiang, T. Low, K. Chang, M. I. Katsnelson, and F. Guinea, Phys. Rev. Lett. **110**, 046601 (2013).
[55] F. Zhai and H. Q. Xu, Appl. Phys. Lett. **88**, 032502 (2006).
[56] Á. Bácsi and A. Virosztek, Phys. Rev. B **87**, 125425 (2013).
[57] Y. Song and H. Dery, Phys. Rev. Lett. **111**, 026601 (2013).